Computer Methods in Biomechanics and Biomedical Engineering, 2013
Vol. 16, No. 2, 198–216, http://doi/dx/org/http://dx.doi.org/10.1080/10255842.2011.615743

CFD analysis of the human airways under impedance-based boundary conditions: application to healthy, diseased and stented trachea

M. Malvè[a,b]*, S. Chandra[c], J.L. López-Villalobos[d], E.A. Finol[c], A. Ginel[d] and M. Doblaré[a,b]

[a]*Group of Structural Mechanics and Materials Modeling (GEMM Group), Aragón Institute of Engineering Research (I3A), Universidad de Zaragoza, C/María de Luna s/n, E-50018 Zaragoza, Spain;* [b]*Centro de Investigación Biomédica en Red en Bioingeniería, Biomateriales y Nanomedicina (CIBER-BBN), C/Poeta Mariano Esquillor s/n, 50018 Zaragoza, Spain;* [c]*Institute for Complex Engineered Systems (ICES), Carnegie Mellon University, 5000 Forbes Avenue, Pittsburgh, PA 15213, USA;* [d]*Department of Thoracic Surgery, Hospital Virgen del Rocío, Avenida de Manuel Siurot s/n, E-41013 Seville, Spain*

(*Received 9 November 2010; final version received 16 August 2011*)

A computational fluid dynamics model of a healthy, a stenotic and a post-operatory stented human trachea was developed to study the respiration under physiological boundary conditions. For this, outflow pressure waveforms were computed from patient-specific spirometries by means of a method that allows to compute the peripheral impedance of the truncated bronchial generation, modelling the lungs as fractal networks. Intratracheal flow pattern was analysed under different scenarios. First, results obtained using different outflow conditions were compared for the healthy trachea in order to assess the importance of using impedance-based conditions. The resulted intratracheal pressures were affected by the different boundary conditions, while the resulted velocity field was unaffected. Impedance conditions were finally applied to the diseased and the stented trachea. The proposed impedance method represents an attractive tool to compute physiological pressure conditions that are not possible to extract *in vivo*. This method can be applied to healthy, pre- and post-operatory tracheas showing the possibility of predicting, through numerical simulation, the flow and the pressure field before and after surgery.

Keywords: CFD; trachea; bifurcation; impedance; stenosis; stent

1. Introduction

The study of air exchange during breathing, sneezing and coughing plays an important role in medicine and biomedical engineering. Due to the individual characterisation and the complexity of the human lungs, the correct fluid mechanics of the gas exchange process remains a challenge. Even though recent advances in computed resources combined with numerical algorithms and medical imaging offer the possibility of studying almost entire lung models with their complex geometry, the flow patterns through the human airways are still on study. Most of the published works on the respiratory system analysed the airflow pattern using idealised (Horsfield et al. 1971; Weibel 1963) or approximated airway geometries (Calay et al. 2002; Nowak et al. 2003; Ma and Lutchen 2006; Gemci et al. 2008). Only a few were based on accurate airway geometries obtained from computed tomography (CT) or magnetic resonance (Zhang and Lessmann 1996; Liu et al. 2002, 2003; Zhang and Kleinstreuer 2002; Jayaraju et al. 2007; Freitas and Schröder 2008; Luo and Liu 2008; Nithiarasu et al. 2008). While these studies (both using simplified or real geometries) considered the airways as completely rigid, neglecting then the high muscular deflections of the trachea (Kim and Iglesias 1989; Kim et al. 1989; Balashazy et al. 1996; Calay et al. 2002; Nowak et al. 2003; Ma and Lutchen 2006; Yang et al. 2006), more recently, fluid–solid interaction (FSI) studies in lower airway geometries done for simplified models/geometries, tracheal tube and single or multiple bifurcations (Roberts et al. 1998; Heil 1999; Heil and White 2002; Hazel and Heil 2003; White and Heil 2005; Koombua and Pidaparti 2008; Wall and Rabczuk 2008; Malvè et al. 2010; Malvè, Pérez del Palomar, Trabelsi et al. 2011; Malvè, Pérez del Palomar, Mena et al. 2011).

On oral/laryngeal flow dynamics, studies were focused mainly on studying the influence of glottis aperture on the tracheal flow and particle deposition in idealised (Matida et al. 2004; Brouns, Verbanck et al. 2007; Xi and Longest 2007) or realistic mouth–throat geometries (Zhang et al. 2002; Jayaraju et al. 2007; Lin et al. 2007). In particular, Lin et al. (2007) studied the dependence of airflow in the intrathoracic airways on the complex pharyngeal and laryngeal geometry. They revealed that a high-speed laryngeal jet, which was skewed with respect to the tracheal centreline, was formed as the flow passes through the glottis. The effect of this turbulent jet on the tracheal flow was also analysed by Xi and Longest (2007), Xi and

*Corresponding author. Email: mmalve@unizar.es

Longest (2008), Xi et al. (2008) and experimentally studied by Corcoran and Chigier (2000) using Doppler interferometry.

With regard to tracheal pathologies, Cebral and Summers (2004) showed how virtual bronchoscopy can be used to study anatomically realistic airway models. Sera et al. (2003) investigated the mechanism of wheeze generation with experiments conducted on a rigid and an extensible realistic CT-based stenotic tracheal model. Moreover, Brouns, Jayaraju et al. (2007) presented a numerical model of a healthy trachea in which different stages of artificial stenosis were imposed, with the aim to understand how different degrees of stenosis affect the local pressure drop. Patients with tracheal airway stenosis often report a relative sudden appearance of breathing impairment, which after admission in the clinic, usually causes the airway stenting intervention in relatively urgent setting. Although after prosthesis implantation, patients gain around 50% of breathing capability, other problems such as coughing difficulties may take place because of the increased rigidity of the tracheal wall due to the presence of prosthesis (Brouns, Jayaraju et al. 2007; Sun et al. 2008), stent migration, inflammatory granulation tissue, formation and accumulation of mucus (Sun et al. 2008). In particular, silicone stents have a small inner diameter due to its thick wall, thus increasing the risk of mucus plugging (Sun et al. 2008). For this reason, a better understanding of the healthy and pathological tracheal flow and of the distinct features of tracheobronchial stents through computational fluid dynamics (CFD) analysis may be necessary to improve clinical outcomes. Despite this importance, we could not find any previous work on respiratory flow through stented trachea.

For these CFD or FSI simulations, the choice of the boundary conditions is critical. While using appropriate inlet velocity or flow conditions at the entrance of the trachea, numerical studies only roughly approximated the impedance of the peripheral bronchi to the airflow through the respiratory system at the outlets, by means of time-dependent (Nowak et al. 2003; Wall and Rabczuk 2008), zero pressure (Liu et al. 2002, 2003; Luo and Liu 2008) or simply outflow conditions (Liu et al. 2002; Nowak et al. 2003; Brouns, Jayaraju et al. 2007). Only the work of Elad et al. (1998) proposed a nonlinear lumped-parameter model to study the dependency of airflow distribution in asymmetric bronchial bifurcations on structural and physiological parameters. There was considerable work in the area of lung impedance, even commonly related to 1D transmission line models (Suki et al. 1993). Only recently, Wall et al. analysed the impact of impedance-based conditions on healthy lungs, modelling the airflow by means of using a structured tree to represent the non-reconstructed airways geometry (Comerford, Bauer et al. 2010; Comerford, Foerster et al. 2011; Wall et al. 2010).

In previous studies (Malvè, Pérez del Palomar, Chandra, Lopez-Villalobos, Mena et al. 2011; Malvè, Pérez del Palomar, Chandra, Lopez-Villalobos, Finol et al. 2011), we used impedance-based conditions for analysing the inspiration flow, stresses and strains of a healthy, a pathological and a stented trachea using FSI approach. In this study, we analysed a healthy, a diseased and a post-operatory human trachea using CFD approach assuming rigid walls. Using these models, as boundary conditions, we computed structured tree impedance-based pressure waveforms through a method originally developed for the cardiovascular system by Olufsen (1999), Olufsen et al. (2000), extended by Steele et al. (2007) and applied by Comerford et al. to the pulmonary system. Different from Comerford, Bauer et al. (2010), Comerford, Foerster et al. (2010), we started the impedance computation from patient-specific healthy, diseased and post-operatory spirometries, which give crucial information about the pulmonary capacity of the patient, especially for a diseased patient, before and after prosthesis implantation. Comparing the results obtained using the impedance pressure conditions with those obtained with other types of traditional outflow conditions we found different computed intratracheal pressures, as obtained by Comerford et al. (2010b) for approximated healthy and mechanical respiration. Moreover, we showed how the developed structured tree outflow conditions can be applied to analyse the flow patterns of a human healthy trachea in comparison with human stenosed and post-operatory tracheas modelling the bronchial system absent in the computational domain. The final aim of our work was to develop the first step into the generation of a numerical tool that is able to simulate and classify the tracheal airflow which, in the future, may help to decide, if surgery is necessary, which surgical method is more suitable.

2. Materials and models

2.1 Computational grid and airflow modelling

First we modelled two geometries: a healthy and a stenotic trachea. Then, for the diseased patient we modelled two different cases that correspond to the trachea before and after surgery. The finite element model (FEM) of the healthy human trachea was created from CT images corresponding to a 70-year-old healthy man, whereas the stenotic tracheal model used CT images of a 56-year-old patient. The DICOM files from the scanned images were segmented using a commercial software MIMICS© (Materialise Technologielaan, Leuven) and clear pictures of black internal cavities were obtained. In Figure 1, the three considered patient-specific models are shown. An IGES file of the segmented geometries was created to construct the associated computational grids. For both geometries, a full tetrahedral element mesh was generated

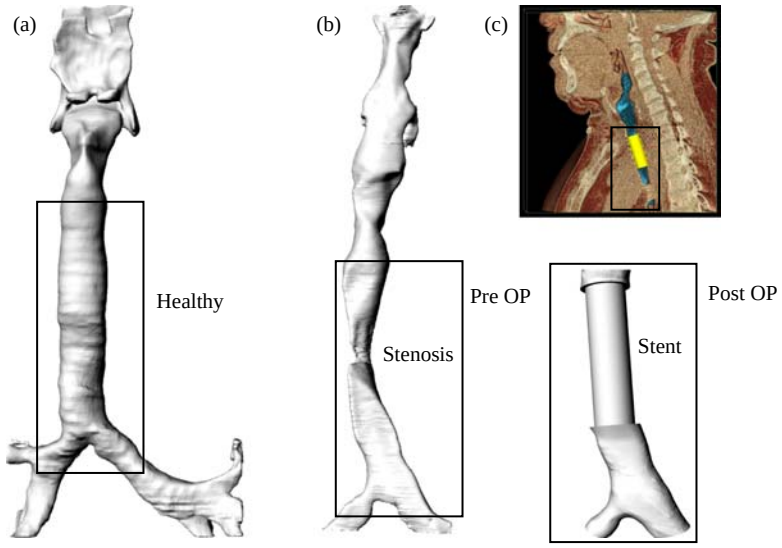

Figure 1. Geometry model of the healthy (a), stenotic pre-operatory (b) and post-operatory trachea (c) (Malvè, Pérez del Palomar, Chandra, Lopez-Villalobos, Mena et al. 2011; Malvè, Pérez del Palomar, Chandra, Lopez-Villalobos, Finol et al. 2011) (the considered parts for the FEMs are squared in black).

using the commercial software Icem CFD© (Ansys, Inc., Software, Canonsburg, PA, USA). The post-operatory geometry was created starting from the stenotic geometry inserting a Dumon (1990) prosthesis. This prosthesis is a radio-opaque silicone tube with a smooth inner surface the dimensions of which in this case are length, 100 mm, diameter, 10 mm and thickness, 2 mm. From the image shown in Figure 1(c), which was created at the stage of pre-operatory planning inserting the Dumon stent in the diseased trachea, the length and the position of the stent with respect to the diseased geometry were detected. The stent was modelled as a perfect cylinder and then introduced in the diseased geometry with the help of a CAD software (Rhinoceros, McNeel & Associates, Indianapolis, IN, USA). Finally, the prosthesis junctions were adjusted to the tracheal walls in order to approximate the internal surface of the stented tracheal geometry as much as possible. However, the stent external diameter is normally higher than the tracheal diameter in order to guarantee perfect adhesion between prosthesis and tracheal walls. The geometry after prosthesis implantation was finally meshed in the same way and with the same aforementioned software.

The total number of tetrahedral elements was around 500,000 for all geometries. In every grid, a boundary layer mesh was generated. To ensure that the results were insensitive to the computational grid size, a sensitivity study was carried out. Four different meshes of 250,000, 500,000, 700,000 and 900,000 elements were tested. Velocity profiles at peak flow during inspiration were studied to ensure that the results at the highest Reynolds number were grid independent, as done in other works (Calay et al. 2002). The airflow was supposed Newtonian ($\rho = 1.225\,\mathrm{Kg/m^3}$, $\mu = 1.83 \times 10^{-5}\,\mathrm{Kg/m\,s}$) (Calay et al. 2002) and incompressible under unsteady conditions. Flow was assumed turbulent for the analysed cases since the Reynolds number at peak flow ($Re_{\mathrm{healthy}} = 30{,}000$, $Re_{\mathrm{stenosis}} = 10{,}000$, $Re_{\mathrm{stent}} = 15{,}000$), based on the median tracheal section, was greater than the laminar limit ($Re_{\mathrm{laminar}} \approx 2000$; Levitzky 2003).

2.2 *Governing equations and numerical method*

The governing equations for tracheal airflow are the Navier–Stokes formulation with the assumptions of turbulent flow. These equations govern the principles of mass and momentum conservation for the mathematical description of airflow and are represented in a simplified vector form as (Oertel 2004)

$$\nabla\cdot\mathbf{v} = 0, \tag{1}$$

$$\rho_f \frac{\partial \mathbf{v}}{\partial t} + \rho_f(\mathbf{v}\cdot\nabla)\mathbf{v} - \nabla\cdot\tau = \mathbf{f}^B, \tag{2}$$

where ρ_f is the airflow density, $\mathbf{v}$ is the airflow velocity vector and τ is the stress tensor (Bathe and Zhang 2004), expressed as

$$\tau = -p\mathbf{I} + 2\mu\mathbf{d}, \tag{3}$$

$$\mathbf{d} = \frac{1}{2}\left(\nabla\mathbf{v} + \nabla\mathbf{v}^T\right), \tag{4}$$

where p is the airflow pressure, $\mathbf{I}$ is the second-order unit tensor, μ is the airflow viscosity and $\mathbf{d}$ is the strain rate. For the airflow analysis, the body force per unit volume $\mathbf{f}^B$ can be neglected.

The Petrov–Galerkin formulation with subspaces V_h and W_h of V and P_h and Q_h of P was used to interpolate the flow conditions over the elements; in particular, the formulation used was of Bathe and Zhang (2002): for a given domain Ω, find $\mathbf{v} \in V_h$, $p \in P_h$ such that for all $\mathbf{w} \in W_h$ and $q \in Q_h$

$$\int_\Omega q\nabla\cdot(\rho_f\mathbf{v}) = 0, \tag{5}$$

$$\int_\Omega \mathbf{w}\left[\frac{\partial\rho_f\mathbf{v}}{\partial t} + \rho_f(\mathbf{v}\cdot\nabla)\mathbf{v} - \nabla\cdot(\pi(\mathbf{v},p))\right]\mathrm{d}\Omega = 0, \tag{6}$$

assuming that the flow problem is well posed in the Hilbert spaces V and P. For a complete description of the introduced subspaces V_h, W_h, P_h and Q_h see Bathe and Zhang (2002).

Since turbulent flow is assumed for all analysed cases, and taking into account the limitations of using the turbulence $K-\varepsilon$ model to its modelling, as documented in Jayaraju et al. (2007), Matida et al. (2004, 2006), the $K-\omega$ model was used to modify the air viscosity. In particular in the Navier–Stokes equations, the viscosity μ was substituted by $\mu_0 = \mu + \mu_\mathrm{t}$ where μ_t is the turbulent viscosity that is expressed as

$$\mu_\mathrm{t} = \alpha\rho_f\frac{K}{\omega}, \tag{7}$$

where α is a constant of the model, expressed as a function of the Reynolds number (Bathe 2006). The variable ω is called specific dissipation rate of turbulence. This is related to the so-called kinetic energy and the rate dissipation of the turbulence K and ε defined as follows:

$$\omega \sim \frac{\varepsilon}{K}, \tag{8}$$

with

$$K = \frac{1}{2}\overline{\mathbf{v}'\cdot\mathbf{v}'}, \quad \varepsilon = \frac{\mu}{\rho_f}\overline{(\nabla\mathbf{v}')\otimes(\nabla\mathbf{v}')}, \tag{9}$$

where $\mathbf{v}'$ is the fluctuating velocity. A complete description of this turbulence model may be found in Bathe.

The governing equations were solved with the FEM. The finite element equations were obtained by establishing a weak form of the governing equations using the Galerkin procedure (Bathe 2006). The continuity equation and the momentum equation were weighed with the virtual quantities of pressure and velocities. The governing equations were integrated over the computational fluid domain. The fluid domain employs special flow-condition-based-interpolation available in the commercial software ADINA R&D, Inc. (Watertown, MA, USA; Bathe 2006). For the present simulations, a time step size of 0.0001 s was used. This was estimated as a compromise between the required computational time and the necessity to catch the most important airflow features. As iteration method we used full Newton–Raphson with a sparse matrix Gaussian solver (Bathe 2006). Finally, convergence was assessed setting a residual relative tolerance of 10^{-5}.

Air is a compressible fluid. However, it is possible to establish an analogy between incompressible flow in a compliant tube and compressible flow in a rigid tube. Tracheal wall was in fact assumed rigid. In general, for an idealised pulsatile airflow in a rigid pipe, pressure and velocity oscillate with the same frequency so that at different axial positions along the tube, airflow must respond *in unison* to the change in pressure (Zamir 2000). At all axial positions, as the pressure changes, the velocity profile changes in response simultaneously at every axial location (the fluid moves *in bulk* (Zamir 2000)). On the contrary, as the pressure changes in a compliant pipe, the velocity variation only acts locally because it can stretch the pipe. The stretched section of the tube recoils and pushes the change in pressure downstream. This phenomenon generates a wave that travels down the tube. In case of rigid pipe, there was no wave travelling. The wave speed is a function of the Young modulus of the tube wall, the tube thickness, the diameter of the tube and the air density. When this density is not constant then changes in pressure lead to compression and expansion of the fluid within the pipe, which provides other wave propagation mechanisms that can also occur in a rigid tube (Zamir 2000).

The assumption of constant air density for the present work is due to the computed airflow velocities. Moreover, previous CFD studies on respiratory system (Calay et al. 2002; Ma and Lutchen 2006; Lin et al. 2007; Luo and Liu 2008; Wall and Rabczuk 2008; Comerford et al. 2010b), even modelling airflow turbulence, assumed constant air density. This confirms that incompressible airflow was largely used and accepted in the literature.

Despite this assumption, although the tracheal wall was assumed rigid for the performed CFD simulations, as will be explained later, the structured tree in which pressure waveforms were computed from the impedance was built through compliant circular tubes in which air is assumed incompressible and Newtonian, and the flow, axisymmetric. This means that in the structured tree we considered the airflow as incompressible along deformable vessels. The numerical model consists of two parts: the upstream domain (trachea and main bronchi) which was assumed as rigid with incompressible airflow and the downstream domain (binary tree) which was assumed as compliant with incompressible airflow. The same approach was applied by Comerford, Bauer et al. (2010), Comerford, Foerster et al. (2011). While tracheal tract and main bronchi are supposed rigid, the pressure waveforms are computed through a compliant tree. One might argue that this is not completely physiologically correct. The purpose of the impedance-based conditions was to provide

suitable physiological pressure waveforms for numerical analysis in the human lungs. This was achieved by considering the impedance tree as compliant, which is physiologically true. These obtained conditions were later applied to the 3D model. Although the approximation of rigid wall was made, the used physiological boundary conditions may provide improvement in the flow pattern evaluation. Many studies on the contrary (Lin et al. 2007; Freitas and Schröder 2008; Gemci et al. 2008; Luo and Liu 2008) assume non-flexible models and use simplified boundary conditions that may strongly affect the results.

2.3 Boundary conditions

Due to the very complex lung geometry, boundary conditions are a critical factor in the study of the flow through human airways. Although some studies used the zero-pressure condition at the outlets of the respective truncated generation (Liu et al. 2002, 2003; Nowak et al. 2003; Ma and Lutchen 2006; Luo and Liu 2008; Nithiarasu et al. 2008), the pressure at each outlet should be known a priori, reflecting the effect of the truncated generation resistances (Gemci et al. 2008). An alternative approach could be by setting the flow ratios in each tracheal branch (Horsfield et al. 1971; Nowak et al. 2003). Ma and Lutchen (2006) attempted this but obtained inaccurate pressure values at the 6th lung generation (Gemci et al. 2008). Gemci et al. (2008) modelled an almost complete anatomical replica of the pulmonary tree down to the 17th generation, assuming the outflow condition $p = 0$. Only recently, impedance conditions were computed for normal breathing and mechanical ventilation and applied to a 3D healthy lung model (Comerford, Bauer et al. 2010; Comerford, Foerster et al. 2011).

In this work, starting from patient-specific spirometries done on both patients (before and after the surgery for the diseased patient), we computed the impedance-based pressure waveforms by means of the procedure developed by Olufsen (1999), Olufsen et al. (2000), explained in the next section. The spirometry is a forced breathing test which consists in enforcing the respiration, blowing off air after a long deep inspiration. It is performed in order to measure the pulmonary dimensions, pulmonary flow, possible bronchial obstructions and, in particular, to get the percentage of pulmonary capacity acquired after stent implantation for the diseased patient.

2.4 The fractal network

In this work, we modelled the non-reconstructed airways as a structured fractal network. In the network, we predicted physiological airflow and pressure profiles. This model consisted of two parts: the trachea, the right and left main bronchus, and the structured binary trees (one each bronchus) that represent the lung bronchial networks. These were attached to the left and right main bronchi. In the fractal network, the airflow and pressure were calculated using the incompressible axisymmetric Navier–Stokes equations for a Newtonian fluid. This can be considered a reasonable assumption as documented in Olufsen (1999), Olufsen et al. (2000) for cardiovascular system and Comerford, Bauer et al. (2010), Comerford, Foerster et al. (2011) for pulmonary system. A 1D model was obtained integrating these equations over the cross-sectional area of each bronchial segment, in the same way as Olufsen (1999), Olufsen et al. (2000) had developed for each blood vessel. As for the blood vessels, the bronchi were modelled as a binary asymmetric-structured tree in which each branch was approximated by a straight compliant segment. The non-reconstructed airways were modelled using a 1D approach previously used for the arterial flow by Olufsen (1999), Olufsen et al. (2000). This approach was modified in order to model the human lung tree. The linearised flow equations are described as follows:

$$\frac{\partial A}{\partial t} + \frac{\partial q}{\partial x} = 0, \tag{10}$$

where p is the pressure, A is the bronchial cross-sectional area and q is the flow rate in the x-direction and

$$\frac{\partial u_x}{\partial t} + u_x \frac{\partial u_x}{\partial x} + u_r \frac{\partial u_x}{\partial r} + \frac{1}{\rho}\frac{\partial p}{\partial x} = \frac{\nu}{r}\frac{\partial}{\partial r}\left(r\frac{\partial u_x}{\partial r}\right), \tag{11}$$

where u_x is the velocity in the x-direction, t is time, p is pressure, ρ is the density, ν is the viscosity and r is the bronchial radius.

The linearised 1D momentum equation was modified with respect to the case of arteries using the appropriate air density and viscosity instead of those of the blood. The approximation of linearised 1D momentum equation for the pulmonary tree is reasonable as documented in other works (Comerford, Foerster et al. 2010) due to the high wave speed. Pulmonary flow is not well modelled using 1D flow equations in the upper portion of the airways due to the associated recirculatory flow phenomena caused by the bifurcations. For this reason, we attached the 1D structured tree to the 3D CT-reconstructed model. In particular, two trees were built one for each bronchus. Pressure waveforms computed recursively from alveolar level to the top of the tree (left/right tree root) were later applied to the model bottom regions. In addition, velocity airflow was imposed to the model inlet. Velocity, which is extracted from the spirometry and adapted through the inlet diameter, was applied through a flat profile. The airways network resulted in a series of bifurcations composed of a series of parent and daughter bronchi, as shown in Figure 2. In the tree, each parent bronchus

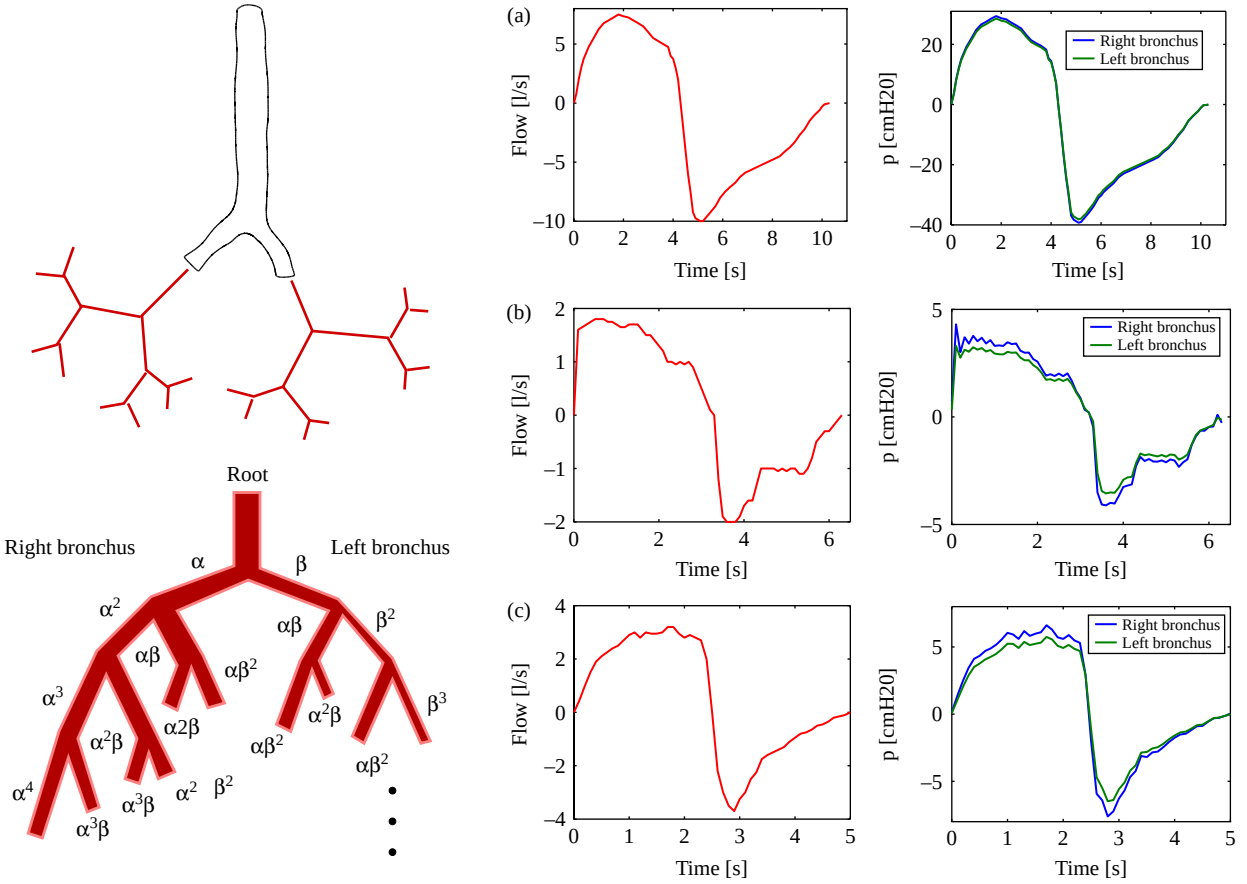

Figure 2. The structured tree [adapted from Olufsen (1999)]: at each bifurcation the radii of the daughter bronchi are scaled by the factors α and β. On the right side, input airflow and computed pressure waveforms of (a) the healthy, (b) stenotic and (c) post-operatory trachea are shown (Malvè, Pérez del Palomar, Chandra, Lopez-Villalobos, Mena et al. 2011; Malvè, Pérez del Palomar, Chandra, Lopez-Villalobos, Finol et al. 2011).

bifurcates into two daughter bronchi following a scaling guided by the asymmetry scaling factors α and β of the root parent r_{root}, according to Equation (12).

$$r_{i,j} = \alpha^i \beta^{j-i} r_{\text{root}}. \tag{12}$$

For each model (healthy, diseased and after prosthesis implantation), assuming separately the left and the right bronchus as root of the tree, we created two asymmetric respiratory networks each corresponding to the left and the right lungs (see Figure 2). In this way, each CT-reconstructed geometry possesses two bronchial networks, one for each bronchus. These trees are different from each other since these are created starting from different bronchus radii. Each fractal tree was created in fact starting from the outlet radius of each tracheal bronchus. The structured tree continues branching until the radius of any bronchial segment is less than the given minimum values r_{min}, as, for instance, the alveolar radius (10–100 μm) in which we assumed zero impedance. Although we know that during inspiration and expiration the alveolar pressure varies sinusoidally between ± 1 cm H_2O (Levitzky 2003), the assumption of zero impedance at the alveolar radius was clearly more appropriate than the assumption of zero pressure applied in other works at intermediate generations (Liu et al. 2002, 2003; Ma and Lutchen 2006; Luo and Liu 2008; Nithiarasu et al. 2008). A more realistic model with a physiological impedance at alveolar level was left for further studies. Asymmetry ratios of the bronchi (Latourelle et al. 2001) were first defined as

$$\eta = \frac{(r_0)_{d_1}^2 + (r_0)_{d_2}^2}{(r_0)_{\text{pa}}^2}, \tag{13}$$

and

$$\gamma = \left(\frac{r_{0_{d_2}}}{r_{0_{d_1}}}\right)^2, \tag{14}$$

where r_{0d_1} and r_{0d_2} are the radii of the daughter bronchi and r_{pa} is the radius of the parent bronchus, while η, the area ratio, and γ, the asymmetry ratio, are related to each

Table 1. Parameters used to describe the airways tree.

Radius (μm)	α	β	ξ	γ	η
$200 < r < 50$	0.8	0.67	2.33	0.7	1.1

Note: as in Olufsen et al. (2000), α and β are kept constant during the tree scaling.

other through the expression (Olufsen 1999):

$$\eta = \frac{1+\gamma}{(1+\gamma^{\xi/2})^{2/\xi}}. \tag{15}$$

Consequently, if the asymmetry ratio γ and the power exponent ξ are known, the area ratio η can be calculated. The value of γ widely varies from humans to dogs and rodents as documented by Latourelle et al. (2001). For this study we assumed γ as 0.7, extracted by Yeh et al. (1979), Horsfield and Woldenberg (1989), Li et al. (2007). Moreover, using a power $\xi = 2.33$, fixed, taking into account that the flow is turbulent (Murray 1926; Olufsen 1999; Zamir 2000), we computed an area ratio of $\eta = 1.1$. Using these parameters, the scaling parameters were obtained from the following expressions:

$$\alpha = (1+\gamma^{\xi/2})^{-1/\xi}, \quad \beta = \alpha\sqrt{\gamma}. \tag{16}$$

The values of α and β can be directly computed using these equations. It has to be noted that in this study we did not divide the network into three sections as done by Steele et al. (2007) so that the scaling parameters were kept constant along the tree for all computed trees (healthy, diseased and post-operatory). The estimated values of α and β agree with those found in the literature for healthy human and ovine lungs (Tawhai et al. 2004; Comerford, Bauer et al. 2010; Comerford, Foerster et al. 2010). The parameters used to scale the fractal tree are shown in Table 1.

2.5 *Impedance recursive computation*

Impedance was computed in a recursive manner starting from the terminal branch (Olufsen et al. 2000; Steele et al. 2007) of the structured tree. The details of the recursive calculation are given elsewhere (Olufsen 1999; Olufsen et al. 2000; Steele et al. 2007). Following the same scheme, we evaluated the input impedance at the beginning of each airway daughter $z = 0$ as a function of the impedance at the end of the airway daughter $z = L$:

$$Z(0,\omega) = \frac{ig^{-1}\sin(\omega L/c) + Z(L,\omega)\cos(\omega L/c)}{\cos(\omega L/c) + ig\,Z(L,\omega)\sin(\omega L/c)}, \tag{17}$$

where L is the bronchial segment length, $c = \sqrt{s_0(1-F_J)/(\rho_f C)}$ is the wave-propagation velocity, $g = \sqrt{CA_0K/\rho_f}$ and

$$Z(0,0) = \lim_{\omega\to 0} Z(0,\omega) = \frac{8\mu l_{\mathrm{rr}}}{\pi r_0^3} + Z(L,0),$$
$$F_J = \frac{2J_1(w_0)}{w_0 J_0(w_0)}, \tag{18}$$

being $J_0(x)$ and $J_1(x)$ the zeroth and first-order Bessel functions with $w_0 = i^3 w$, $w^2 = \rho r_0^2\omega/\mu$, i the complex unity and w the Womersley number. The compliance C is approximately given by

$$C = \frac{3A_0 r_0}{2Eh}, \quad \frac{Eh}{r_0} = k_1\exp(k_2 r_0) + k_3, \tag{19}$$

with k_1, k_2 and k_3 being known constants obtained by Olufsen (1999), s_0 the cross-sectional area, r_0 the bronchus radius corresponding to the section s_0, h the wall thickness and E the Young modulus of the bronchus.

The length of each daughter segment L is related to the radius r_0 using a constant length-to-radius ratio $l_{\mathrm{rr}} = L/r_0$. This parameter is well known for the vascular network in the literature (Olufsen et al. 2000; Steele et al. 2007). For the human airways, morphometric and anatomic data for humans and rodents are described in Horsfield et al. (1971), Habib et al. (1994), Latourelle et al. (2001), Calay et al. (2002), Yeh et al. (1979), Raabe et al. (1976), Weibel (1963). These works showed that this parameter rapidly varies from the trachea to the bronchioles, till the alveolar level (from around 12 to 2 (Levitzky 2003; Weibel 1963)). Based on these studies, we finally fixed a constant average value of $l_{\mathrm{rr}} = 6$ (Horsfield and Woldenberg 1989; Levitzky 2003; Li et al. 2007; Weibel 1963). At the right side of Figure 2, each spirometry is shown with the corresponding left and right bronchus pressure waveforms.

For the performed impedance recursive calculation, the pressures at both outlets were computed starting from their flow rates, respectively. From the spirometry, the flow rate entering both branches was first computed using the power law (Murray 1926; Olufsen 1999; Olufsen et al. 2000; Steele et al. 2007):

$$r_{0_{\mathrm{pa}}}^{\xi} = r_{0_{\mathrm{d1}}}^{\xi} + r_{0_{\mathrm{d2}}}^{\xi}, \tag{20}$$

where $r_{0_{\mathrm{pa}}}, r_{01}, r_{02}$ and ξ were previously defined. Finally, to minimise the influence of the uniform velocity assumption on the intratracheal flow field, the boundary location was moved upstream from the model inlet; this was done by adding a 5-inlet diameter extension to each model grid. In particular, to take into account the effect of the laryngeal jet on the tracheal flow (Corcoran and Chigier 2000; Brouns, Verbanck et al. 2007; Lin et al. 2007), as done in other studies (Lin et al. 2007; Luo and Liu 2008), the tracheal inlet extension was biased towards the rear wall. At the outlets, in order to reduce the effect of

the truncated generations on the fluid field, a 10-outlet diameter extension for each bronchus was considered. Lastly, at the tracheal walls, the typical no-slip condition was applied.

2.6 Coupling between 3D and 0D domains

Using Equations (17) and (18), it was possible to compute the impedance at the root of each airway as a function of the impedance at the end of each considered airway. The pressure waveform at the root of the 0D model can be obtained using the convolution theorem (Olufsen 1999; Olufsen et al. 2000), i.e. convoluting the impedance with the flow time history at each airway outlet:

$$p(t) = \int_{t-T}^{T} q(t)z(t-\tau)\mathrm{d}\tau, \tag{21}$$

where $p(t), z(t)$ and $q(t)$ are the time-dependent pressure, impedance and flow, respectively. The coupling between 3D and 0D was achieved by applying a spatially uniform pressure at the grid elements of both outlet surfaces of the 3D numerical model. To dump the effect of the spatial uniform pressure at each bronchus, as aforementioned, the model outlets were extended in order to guarantee fully developed flow in the domain. Finally, the applied pressure at each outlet varies with the time, so that at each new time step of the numerical computation, a new constant pressure value is applied at each outlet following the waveforms displayed in Figure 2 – right.

3. Results and discussion

3.1 Intratracheal pressure comparison

To assess the importance of using impedance-based pressure conditions, the pressure field obtained using impedance-based waveforms was compared with those obtained using standard traction-free outflow conditions and imposing the air flow at the outlet through the Murray (1926) law. For this comparison, in all cases the inflow condition showed in Figure 2(a) was used. In Figure 3, the pressure temporal histories at a median section of the trachea are shown for the three types of outflow conditions used. As visible, evident differences can be found especially in the values. In particular, while the traction-free conditions lead to low pressures (5 cm H_2O and 7.5 cm H_2O for peak inspiration and exhalation, respectively), typical of normal breathing (McCool 2006) but not of the used forced breathing, imposing the flow leads to very high values that are not physiological. On the contrary, the impedance conditions lead to a maximal pressure of about 25 cm H_2O during forced inspiration and of about 32 cm H_2O during forced exhalation, which are in the physiological range (Levitzky 2003; McCool 2006). In Table 2, the obtained values are summarised. Comparing literature data and impedance-computed pressures, we can see almost a good agreement during exhalation while a discrepancy of about 10 cm H_2O can be found for the maximal inhalation pressure. On the contrary, traction-free and flow split conditions show high discrepancies when compared with the literature data (Levitzky 2003).

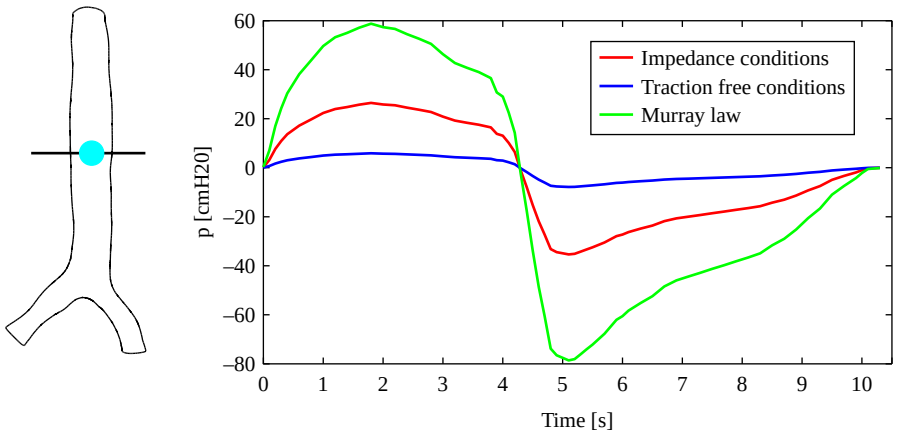

SIMULATION	Impedance	Traction free	Murray
Forced inspiration	25 cmH_2O	4 cmH_2O	60 cmH_2O
Forced expiration	32 cmH_2O	5.5 cmH_2O	78 cmH_2O
LITERATURE	**Impedance**	**Traction free**	**Murray**
Natural inspiration	$\approx 1-1.5$ cmH_2O (13; 41)	≈ 7 cmH_2O (50)	-
Natural expiration	≈ 3 cmH_2O (41)	-	-

Figure 3. Comparison of the temporal pressure history (in cm H_20) at a median tracheal section between different outflow conditions: impedance-based pressure, traction-free and flow split conditions.

Table 2. Comparison of pressures (in absolute value) computed through different boundary conditions at peak flow during forced inspiration and expiration.

Simulation	Impedance	Traction free	Murray
Forced inspiration	25 cm H_2O	4 cm H_2O	60 cm H_2O
Forced expiration	32 cm H_2O	5.5 cm H_2O	78 cm H_2O
Literature	Lung pressure (Levitzky 2003)	–	–
Forced inspiration	≈35 cm H_2O	–	–
Forced expiration	30–25 cm H_2O	–	–

As documented in other studies (Brouns, Jayaraju et al. 2007; Wall et al. 2010), from a physiological perspective the determination and understanding of correct airway pressure drop are crucial for lung mechanics, especially for diseased patients. This aspect reinforces the need to correctly estimate intratracheal pressure by means of applying correct pressure boundary conditions to the numerical model. The impedance method represents an accessible way to determine pressure waveforms that are not possible to get *in vivo*, starting from the intratracheal flow, which can be easily obtained through a standard technique as a spirometry. With the impedance method it would be possible to study the fluid dynamics and, in general, mechanical aspects of the respiration in the upper portion of the airways (such as the tracheal flow in the presence of stenosis or prosthesis), without the necessity to reconstruct the entire lung geometry. Resistance conditions, which could be applied to the terminal outlets of each presented model, should consider in fact a significant number of generations for capturing the fluid dynamics features as documented in Comerford, Bauer et al. (2010), Comerford, Foerster et al. (2010). This is due to the fact that from the small airways comes around 10% of the resistance as reported in Evans and Green (1998), Macklem (1998).

3.2 Healthy trachea

The flow inside the healthy trachea during inhalation and exhalation is shown in Figure 4(a). During inspiration, the trachea shows a strong primary axial flow in which the velocity profile (in the order of 22 m/s) is flattened by the turbulence (see Figure 5(a), (b)). Up to the first bifurcation, named carina, the flow is nearly parabolic, where as after the flow divider, the stream has split as the air moves towards the daughter tubes. In the right main bronchus, a typical secondary swirl-flow is observed that is slightly asymmetric (see Figure 5(a), section 4) as it was found also by Wall and Rabczuk (2008) and by Calay et al. (2002) for a single bifurcation. Also, and as found in other studies (Comer et al. 2001a, 2001b; Nowak et al. 2003; Wall and Rabczuk 2008), the velocity distribution in the right main bronchus is slightly skewed towards the outer wall (see Figure 5(b), section 3). In the left main bronchus, the airflow possesses a high axial component, in which the velocity is in the order of 20 m/s, so that the typical Dean-flow pattern, found by Freitas and Schröder (2008), Luo and Liu (2008), Wall and Rabczuk (2008), is not present (see Figure 5(a), section 3). As documented in Luo and Liu (2008), the secondary flow is induced by the bend curvature and the flow divider. However, the effect of these geometrical factors is not sufficient, in comparison with the axial flow component, to produce the Dean-type pattern (Liu et al. 2002, 2003; Luo and Liu 2008). The reason for that has to be associated with the higher flow rates we used in comparison with other works. It has to be remarked in fact that the present computations impose velocity extracted from a patient-specific spirometry (forced respiration) as inlet condition. In this way a patient-specific flow rate can be correlated with the pulmonary capacity of the patient before and after surgery. On the contrary, previous studies (Liu et al. 2002, 2003; Luo and Liu 2008; Wall and Rabczuk 2008) adopted approximated sinus-shaped velocities for normal breathing and healthy patient. Also, the left main bronchus shows a typical M-shaped velocity profile due to the high velocity field and its particular geometry (Figure 5(b), section 3); this typical distribution is normally associated with a high Reynolds number as documented in Wall and Rabczuk (2008) among others. Also at the flow divider, the velocity profile is M shaped, due to the high Reynolds number and due to the presence of the flow divider. In Figure 5(a) – section 2, the splitting stream is clearly identified.

As documented in other works (Calay et al. 2002; Freitas and Schröder 2008; Wall and Rabczuk 2008), the exhalation flow is regulated by the daughter bronchi. The velocity field possesses a very high axial component almost along the entire geometry: in the main bronchi no secondary flows were found. As a consequence of the asymmetric merging of the two air streams coming from the right and left bronchi, the velocity profile at section 1 in Figure 5(d) was less flattened than at inspiration, even the flow patterns sketched in Figure 5(c) – section 1 and Figure 5(a) – section 1 were quite similar. Finally, the bronchial streams joining at the flow divider, both skewed to the inner and the outer wall, respectively (Figure 5(d), sections 3 and 4), build a parabolic M-shaped profile in axial direction as shown in Figure 5 – section 2, to flow out through the tracheal tube. At the bottom of Figure 5,

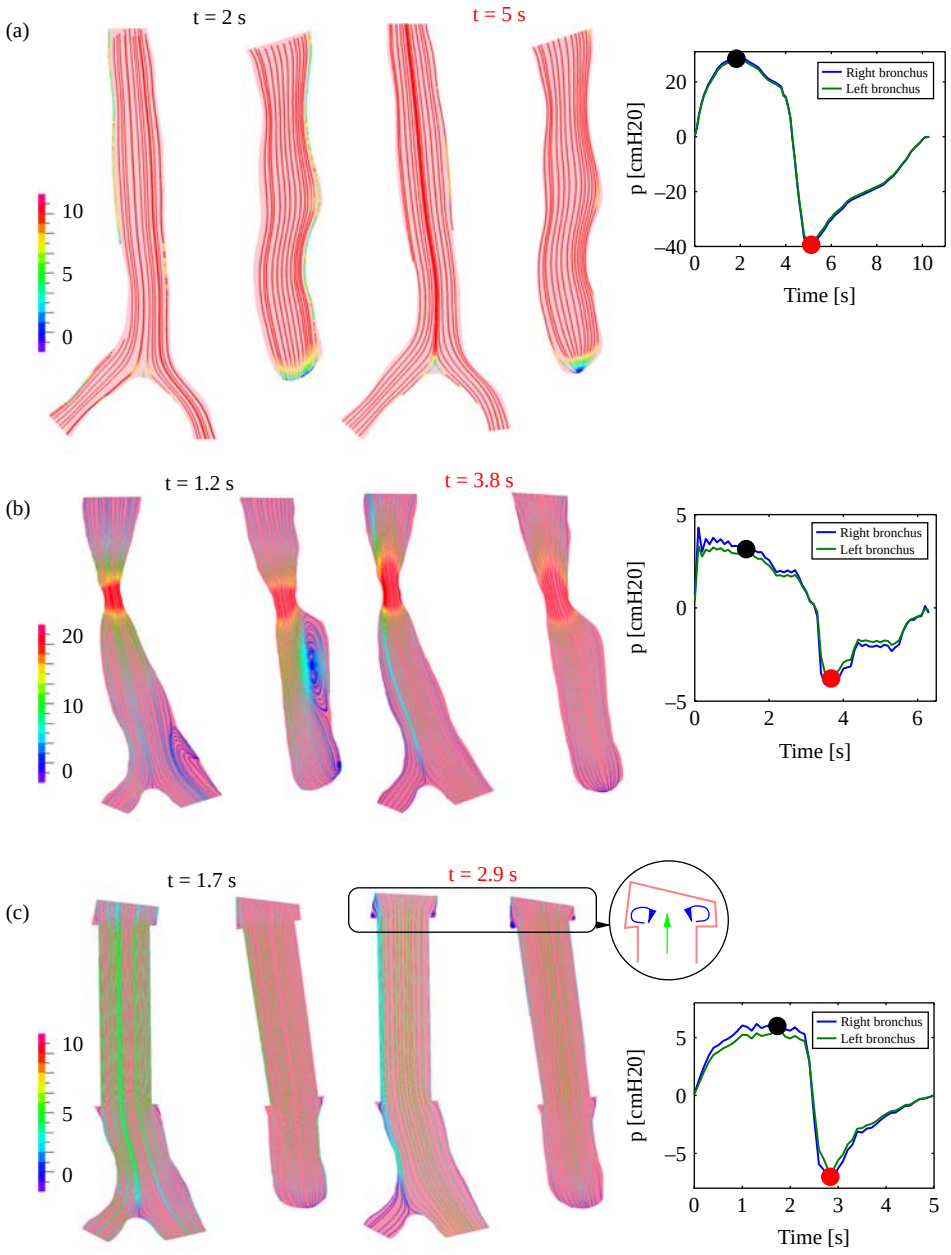

AXIAL VELOCITY	Healthy trachea	Left Bronchus	Right Bronchus
Forced inspiration	$\approx 22\ m/s$	$\approx 19\ m/s$	$\approx 17.5\ m/s$
Forced expiration	$\approx 18\ m/s$	$\approx 17\ m/s$	$\approx 15.5\ m/s$
Natural inspiration	$\approx 8\ m/s$ (27)	$1\ m/s$ (70)	$\approx 1\ m/s$ (70)
Natural expiration	$\approx 1\ m/s$ (18)	$\approx 0.6\ m/s$ (18)	$\approx 0.6\ m/s$(18)
AXIAL VELOCITY	**Stenotic region**	**Left Bronchus**	**Right Bronchus**
Forced inspiration	$\approx 25\ m/s$	$\approx 14\ m/s$	$\approx 10.5\ m/s$
Forced expiration	$\approx 20\ m/s$	$\approx 14\ m/s$	$\approx 12\ m/s$
AXIAL VELOCITY	**Stented trachea**	**Left Bronchus**	**Right Bronchus**
Forced inspiration	$\approx 18\ m/s$	$\approx 13\ m/s$	$\approx 11\ m/s$
Forced expiration	$\approx 16\ m/s$	$\approx 14\ m/s$	$\approx 11\ m/s$

Figure 4. Projected 2D streamlines (in m/s) on frontal and lateral longitudinal sections of (a) the healthy, (b) stenotic, and (c) stented trachea during inspiration (left) and exhalation (right).

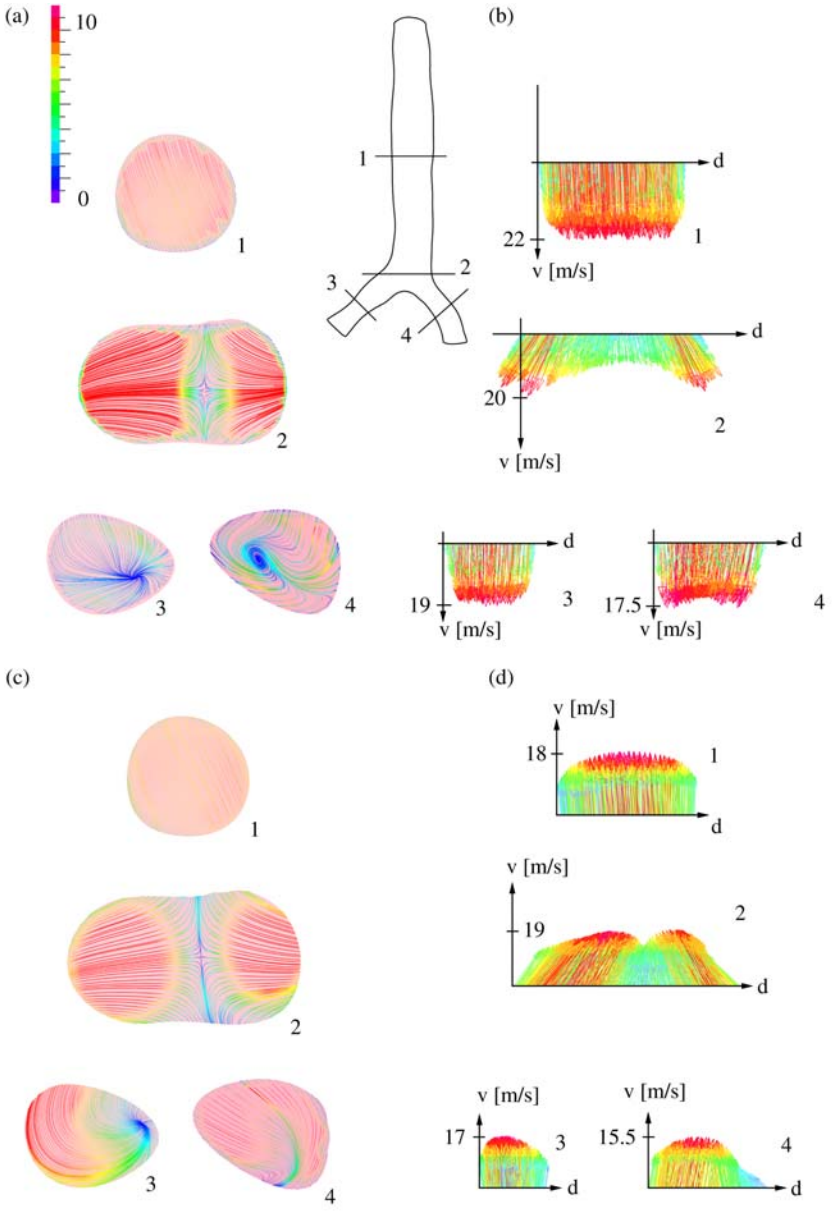

	Healthy trachea	Left Bronchus	Right Bronchus
Forced inspiration	$8\ m/s$	$3\ m/s$	$5\ m/s$
Forced expiration	$7\ m/s$	$9\ m/s$	$8\ m/s$
Natural inspiration (39; 35)	$1-2\ m/s$	$1-2\ m/s$	$1-2\ m/s$
Natural expiration (18)	$0.9\ m/s$	$0.6\ m/s$	$0.6\ m/s$

Figure 5. Projected 2D streamlines (in m/s) on longitudinal sections of the healthy trachea and corresponding velocity profiles at peak flow during inhalation ($t = 2$ s, sub-figures (a) and (b), respectively) and exhalation ($t = 5$ s, sub-figures (c) and (d), respectively). At the bottom of the figure, results are summarised and compared with the literature data given in the table.

computed mean velocities are summarised in the table and compared with the values in the literature. Velocities refer to the section-projected streamlines. It has to be noted that the literature values refer to natural breathing. Axial airflow velocities are summarised at the bottom of Figure 4. As noticeable, there are discrepancies between the computed velocity values and the literature data. Even though these discrepancies are less than one order of

magnitude, these have to be considered relevant. The main reason for this can be found in the different boundary conditions we used in comparison with literature works. Although here inlet velocity conditions were extracted from the flow rates obtained by patient-specific spirometries, in the literature, studies normally apply sinus-shaped velocity waveforms with lower flow rates which approximate normal breathing. The flow rate used for forced breathing in this study rises 8 l/s (see Figure 2(a)). On the contrary, flow rates used in Lin et al. (2007), Freitas and Schröder (2008) and Luo and Liu (2008) were around 1 l/s. This fact is reflected in the computed velocities that are four times higher than the values found in the literature during inspiration and expiration. Discrepancies are also obviously found in the main bronchi. In addition, it has to be noted that the pressure computed with the impedance method is also higher with respect to the literature data (these are functions of the flow rates which are higher). For this reason, there are high differences between the computed intratracheal pressure values and the literature data (see the table at the bottom of Figure 3).

3.3 Stenotic trachea

In the diseased trachea, strong modifications of the local airways flow patterns were found due to the high pressure drop and the elevated wall shear stress (WSS) caused by the stenosis (see Figures 6 and 7). The stenotic geometry shows a higher WSS in the constriction region (with maximum value 15 Pa) as also reported by Cebral and Summers (2004), which causes an increase of about 70% of the WSS registered for the stented trachea (around 1–2 Pa). The observed pressure drop during inspiration was

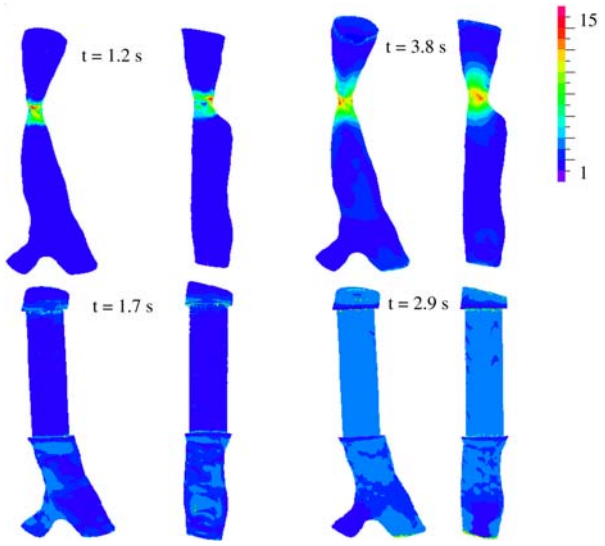

Figure 6. WSS distribution (in Pa) of stenotic (top) and stented trachea (bottom) on frontal and lateral 3D view at peak flow during inspiration (left) and exhalation (right).

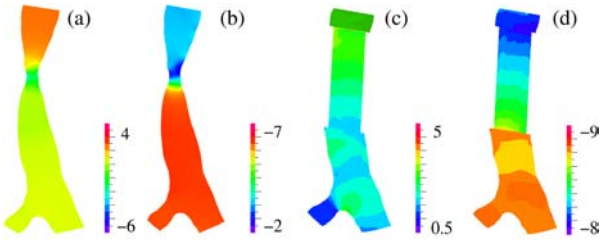

PRESSURE DROP	Stenosed Trachea	Literature
Inspiration	8 cmH_2O	3 cmH_2O (6)
Expiration	5 cmH_2O	4 cmH_2O (9)
PRESSURE DROP	**Stented Trachea**	**Literature**
Inspiration	1.5 cmH_2O	-
Expiration	0.25 cmH_2O	-

Figure 7. Spatial pressure distribution (in cm H_2O) of the trachea before and after prosthesis implantation (sub-figures (a),(b) and (c),(d), respectively) at peak flow during inspiration (sub-figures (a),(c)) and exhalation (sub-figure (b),(d)). At the bottom of the figure, results are summarised and compared with the literature data given in the table.

around 8 cm H_2O, which is higher than that found in the literature (Brouns, Jayaraju et al. 2007). During expiration, the pressure drop is slightly reduced reaching values of 5 cm H_2O (in absolute value). In Table 3, the pressure drops during inspiration and expiration are summarised and compared with the values found in the literature. An exact comparison cannot be made since the flow conditions used in this work and those found in the literature are different.

Although the velocity profile before stenosis is almost axial (around 20 m/s), the highly reduced geometrical cross-section creates a dead fluid zone before bifurcation (see Figure 4) with a longitudinal vortex which influences the flow distribution after the flow divider. This flow distribution is in agreement with the work of Brouns, Jayaraju et al. (2007). Due to the stenosis asymmetry, a high velocity jet results in a skewed velocity profile: the longitudinal vortex is caused by the geometry of the stenosis and from the viscous forces exerted from the resting fluid onto the jet core. In the right and left main bronchi, a local swirl is visible as shown in Figure 8(a) in sections 5 and 6. The fully developed secondary flow results in the skewed velocity profiles inside both main

Table 3. Comparison of the pressure drops computed for the diseased patient at peak flow during forced inspiration and expiration.

Pressure drop	Stenosed trachea	Literature
Inspiration	8 cm H_2O	3 cm H_2O (Brouns, Jayaraju et al. 2007)
Expiration	5 cm H_2O	4 cm H_2O (Cebral and Summers 2004)

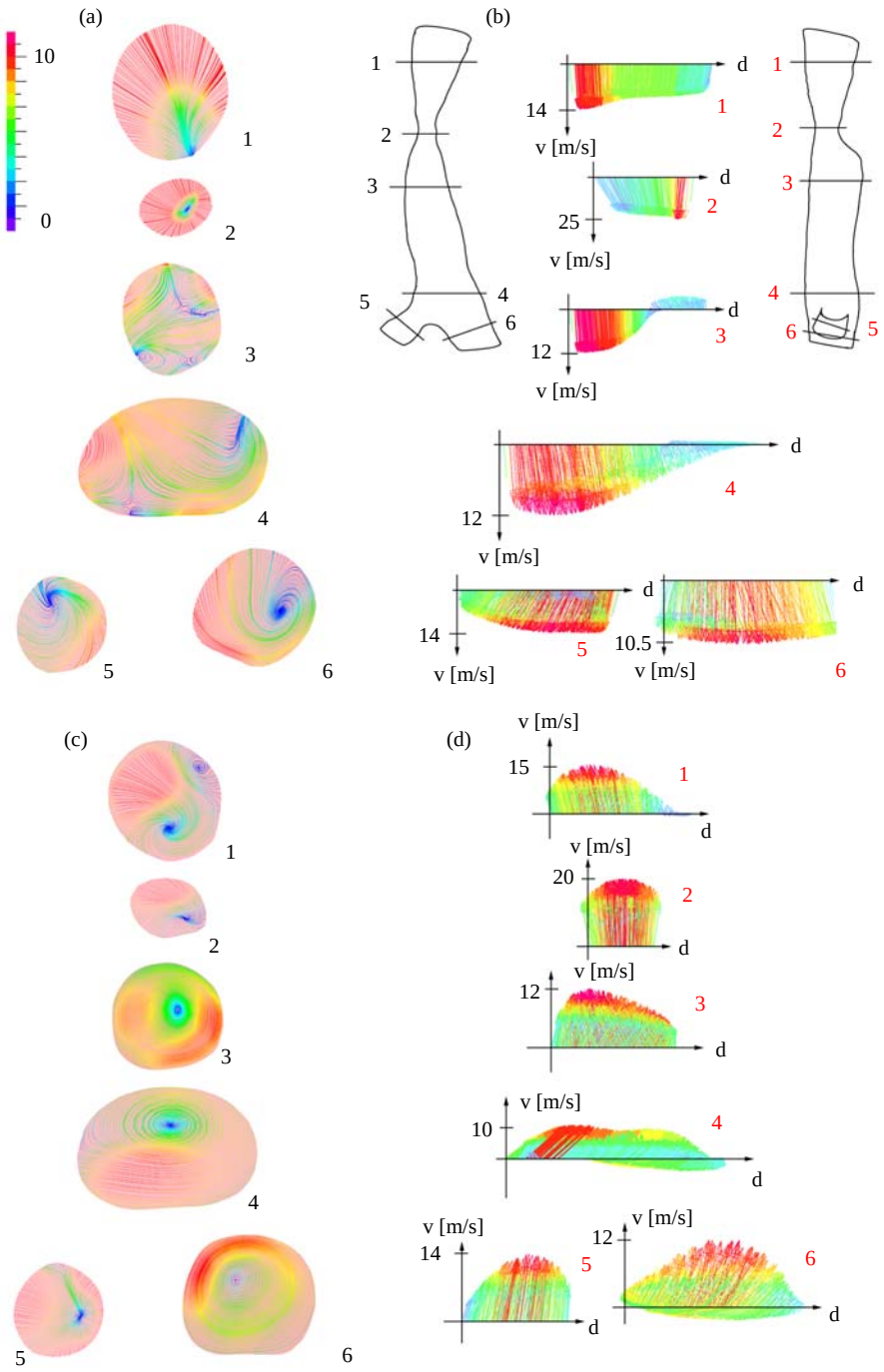

	Diseased trachea	Left Bronchus	Right Bronchus
Forced inspiration	$12\ m/s$	$7\ m/s$	$8\ m/s$
Forced expiration	$9\ m/s$	$7.5\ m/s$	$8\ m/s$
Natural inspiration (6; 56)	$1\ m/s$	$1\ m/s$	$1\ m/s$
Natural expiration (56)	$0.5\ m/s$	$0.2\ m/s$	$0.3\ m/s$

Figure 8. Projected 2D streamlines (in m/s) on longitudinal sections of the stenotic trachea and respective velocity profiles at peak flow during inhalation ($t = 1.2$ s sub-figures (a) and (b), respectively) and exhalation ($t = 3.8$ s, sub-figures (c) and (d), respectively). At the bottom of the figure, results are summarised and compared with the literature data given in the table.

bronchi, both towards the inner wall (velocity profiles 5 and 6 in Figure 8(b)). Moreover, the velocity profiles of sections 3 and 4 (see Figure 8(a), (b)) show some negative components due to the stenotic stream jet and consequently low-velocity vortex inside the trachea.

During expiration, the tracheal flow field looks more intricate than during inspiration. As for the healthy trachea, the exhalation flow is in fact regulated by the two daughters airways. Again two different airflows, coming from the main bronchi, join at the bifurcation. At the constriction, the airflow velocity reaches very high values (20 m/s), as shown in section 2 of Figure 8(d). In the trachea, a swirl flow develops, a cause of the asymmetric flow divider: the swirl flow coming from the right bronchus joins that coming from the left with indentation of the skewed velocity profiles of both main bronchi (see Figure 8(d), sections 4–6). This flow type, visible also in section 3 of Figure 8(c), induces a typical Dean flow in the upper section of the trachea (Figure 8(c), section 1), resulting in a skewed profile with reversed velocity components caused by the stenotic geometry. The same flow patterns in the left and right main bronchi were previously reported by the study of Sera et al. (2003). Our findings qualitatively confirm their experimental work which revealed that vortices downstream of the stenosis were stronger during exhalation flow than during inhalation flow.

Because of the rapid progression of the symptoms in most patients with stenosis, diagnosis and therapeutic decisions are normally based on history, physical examinations and imaging studies (Brouns, Jayaraju et al. 2007). Moreover, there is no standardised approach in the follow-up of patients treated for tracheal stenosis. The performed simulation shows a possible way to evaluate parameters such as pressure drop through the patient-specific stenosis which cannot be assessed *in vivo*, suggesting an alternative valuable diagnostic tool. Finally, at the bottom of Figure 8, computed mean velocities are summarised in the table and compared with the values of the literature for diseased trachea. Velocities refer to the section-projected streamlines. Axial velocities are summarised at the bottom of Figure 4. Also here, as previously discussed, differences between computed values and literature data are visible. Once again, the used flow rates are different from those used by Sera et al. (2003) and Brouns, Jayaraju et al. (2007). In the table at the bottom of Figure 8, we can see one order of magnitude difference between computed values and literature data for inhalation and exhalation. These discrepancies only slightly attenuated in the main bronchi. Also in this case the reason for that is due to the different flow rates used. Finally, differences in pressure drops for the stented trachea are also noticeable (see the table of Figure 7). Pressure drops are more than two times higher for inhalation than the values found by Brouns, Jayaraju et al. (2007). During exhalation, the computed pressure values are in agreement with those found by Cebral and Summers (2004).

3.4 *Post-operatory stented trachea*

The comparison between WSS of the stenotic and stented trachea is sketched in Figure 6. In the figure, it is clearly shown how the WSS after surgery again assumes physiological values (1–2 Pa) with an almost uniform WSS distribution along the stent (see Figure 6). In addition, the post-operatory trachea that showed high pressure drops before surgery now shows a uniform pressure distribution. The flow through the stent, during inhalation, is axial, strongly flattened by the turbulence regime and by the geometry of the stent, as shown in Figures 4(c), 9(a) (section 1). In the right and left main bronchi, there is no secondary flow as shown in Figure 9(a), sections 3 and 4. This is probably due to the geometry of the prosthesis and the high axial velocity inside the trachea (around 18 m/s). Both are in fact more relevant than the bending curvature and than the highly asymmetric flow divider, which in the healthy and stenotic tracheas were responsible for the secondary flows. The velocity profiles are very flattened and slightly skewed to the inner and outer wall, respectively, for the right and left main bronchi. Their computed values at peak flow are 13 and 11 m/s, respectively.

The exhalation flow is slightly different from that of inhalation. The velocity profile through the stent is less flattened than during inspiration as shown in Figure 9(d) at each velocity profile section. The same flow pattern as for the inspiration process is registered at the flow divider (section 2 in Figure 9(c)) where as a secondary flow is visible in the left bronchus (section 3, Figure 9(c)). Moreover, a secondary Dean flow is shown at section 1 of Figure 9(c); this flow pattern results from the stent geometry. The high speed jet (16 m/s) crossing the stent causes in fact a recirculation at the top of the prosthesis, near the tracheal wall (see Figure 4(c)), which is a region predisposed to mucus plugging as reported by Lindenmann et al. (2006) and Sun et al. (2008). The Dumon stent can be in fact affected by mucous obstruction due to the interference of the prosthesis with the tracheal wall. Our hypothesis is that this plugging can initiate from the top surface of the stent. As already discussed in the introduction of this work, mucous accumulation and, more in general, airways obstruction due to prosthesis are typical problems in stenting implantation. In this sense, after a surgical stent implantation, we can confirm that although the patient acquires part of the lost capacity of inspiration and expiration (compare flows in Figure 2(b), (c)), the airflow seems to be the cause of well-known post-operatory problems. Computed mean velocities are summarised at the bottom of Figure 9. Velocities refer to

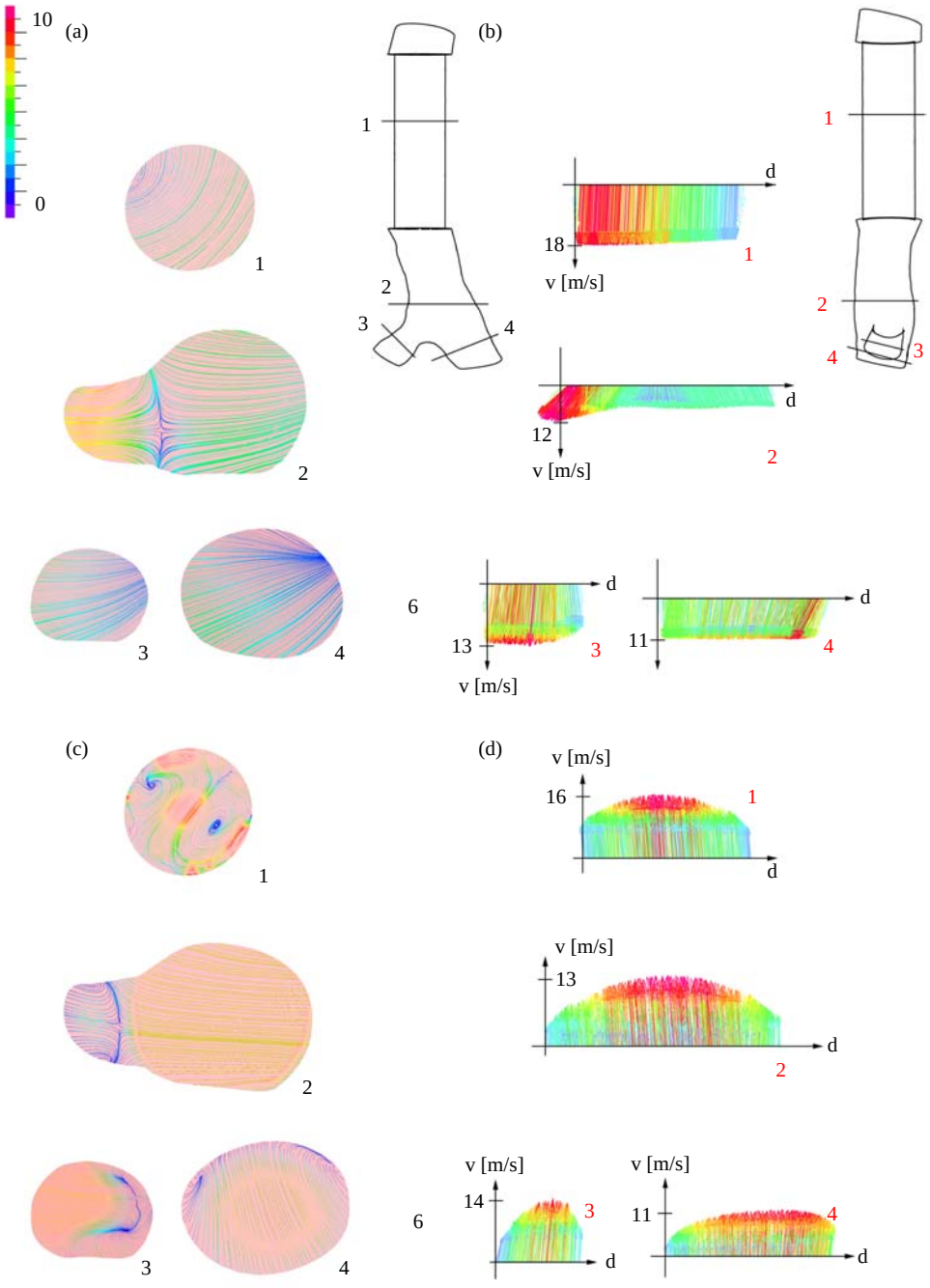

	Stented trachea	Left Bronchus	Right Bronchus
Forced inspiration	5 m/s	2.5 m/s	3 m/s
Forced expiration	10 m/s	7 m/s	6 m/s

Figure 9. Projected 2D streamlines (in m/s) on longitudinal sections of the post-operatory trachea and respective velocity profiles at peak flow during inhalation ($t = 1.7$ s, sub-figures (a) and (b), respectively) and exhalation ($t = 2.9$ s, sub-figures (c) and (d), respectively). At the bottom of the figure, results are summarised in the table.

the section-projected streamlines. Axial velocities are summarised at the bottom of Figure 4.

3.5 Limitations

Although this work contributes to the understanding of the response of a human trachea under different conditions, there are some limitations. In first place, in the modelled patient-specific tracheas we considered only the first bifurcation. Flow structures found in the present work matched well with those found in the literature with similar geometries (Calay et al. 2002). These studies included only one bifurcation and compared the results with those of multiple bifurcations model. They found that one bifurcation is enough to well model the inhalation flow in the trachea and main bronchi. The exhalation flow presents differences due to the different 'inlet boundary conditions' at the daughter airways. In other words, joining airflow coming from one bifurcation neglects airflows previously joined from smaller daughter vessels (flow comes directly from the first bifurcation into the trachea). For more precise results, several bifurcations may be necessary [from 7 up to 17 as documented in Lin et al. (2007), Freitas and Schröder (2008), Gemci et al. (2008), Wall and Rabczuk (2008)]. In addition, the presented trachea–bronchi models are assumed to have rigid walls. Although the numerous CFD studies on human airways are done with this assumption, this could be considered as a limitation, since the trachea shows relative relevant deflections during breathing. Although an FSI approach is promising and pursued in parallel work (Malvè, Pérez del Palomar, Chandra, Lopez-Villalobos, Mena et al. 2011), here we assumed that the CFD solution is not much affected by the tracheal deformations. The CFD approach is largely used to compute flow patterns in the human airways (Tawhai et al. 2004; Brouns, Jayaraju et al. 2007; Gemci et al. 2008; Luo and Liu 2008). Especially the work of Comerford, Bauer et al. (2010), Comerford, Foerster et al. (2010) applied impedance-based conditions, for a rigid wall tracheal model, along a compliant bronchial network. As documented in other studies (Wall and Rabczuk 2008; Xia et al. 2010), there is a general agreement that the influence of deformable tracheal walls is neglectable. For this reason, the assumption of rigid wall can be accepted in the first approximation. Moreover, the geometry of the post-operatory trachea is not patient specific. This was reconstructed by introducing the stent in the stenotic geometry using clinical images. Even in this way we were able to get the real positioning of the prosthesis; in future works, the complete geometry after stent implantation should be reconstructed using post-operatory patient-specific CT images. The geometry of the entire bronchial network was not available for this study. We know that the real bronchial network is very complex so that in the impedance computation, several geometrical approximations were considered. A study of the influence of geometrical parameter of the fractal network on the pressure waveforms (as, for instance, α, β and l_{π}) should be done. Moreover, even using outlet extensions, the flow field through the carina is affected by the truncated generations so that for future work more bifurcations will be considered. As already mentioned, for the recursive computation of the pressure waveforms, we set zero impedance at alveolar level even though the alveolar pressure is not zero but varies from negative to positive pressures (with respect to atmospheric pressure) during breathing. The inclusion of this aspect is possible but left for further studies. Moreover, the presented CFD simulations should be extended and tested to a large number of pathologies and prosthesis types. In this sense, this is the first step of a future classifying work. Finally, this work gives a new insight into the knowledge of the stenting techniques under a fluid dynamical point of view but misses an experimental validation in order to prove the actual predictive capacity of the numerical model. This validation would be carried out in future works.

4. Conclusion

The pulmonary function aspects, specific to each patient airway model, can be revealed using the proposed numerical simulations by applying physiological impedance-based boundary conditions. Physiological pressure conditions inside the bronchial network in fact cannot be obtained through measurements in patients. The impedance method represents an attractive tool to get pressure waveforms, starting from flow measures, which are easy to get *in vivo* through standard techniques such as patient-specific spirometry. The unsteady tracheal airflow was studied under impedance-based boundary conditions and turbulence modelling. Using a single bifurcation, taking into account the impedance of the respiratory system through the use of the mentioned boundary conditions, we obtained physiological flow features which qualitatively agree with previous studies. The combination of medical imaging and CFD analysis allows studying the flow patterns to healthy and pathological tracheas. A comparison between different boundary conditions types showed differences in the computed intratracheal pressures, which are an important parameter to take into account, especially for diseased patients. In particular, imposing the flow at the model outlets or imposing traction-free conditions led to non-physiological pressure values. This supports the importance of using impedance-based conditions. We also showed the possibility to generate a numerical model able to analyse post-operatory situations. Quantification of flow patterns inside different airway geometries such as those with stenotic or stented tracheas could be done before a surgery in order to help surgeons in the choice of

stent type and positioning before surgery. In this sense, the proposed simulations could be useful as pre-operatory planning. As known, CFD (and especially FSI) analyses are computationally time consuming. After the CT images are acquired, we expected a waiting time of few days before the CFD results can be shown. This is still too high if, for example, a patient must be operated in an urgent setting. For this reason, at this moment, the proposed simulations can help the overall effect of a tracheal endoprosthesis on the breathing flow dynamics, while the computational costs represent the first point which must be improved before these can be clinically adopted. In future, such simulations could be used to extract quantities that cannot be assessed *in vivo* as pressure drops and WSS and to derive parameters that can be used as indicators of whether medical intervention is needed. From pressure drop, the degree of stenosis can be in fact be revealed very easily and potential stent positioning and size could be numerically analysed before surgery in order to predict mechanical and clinical consequences of stent implantation. With this aim, FSI analysis of the human trachea before and after prosthesis implantation may also be of interest. For these simulations, pressure information is necessary to correctly compute stresses, strains and deflections. Impedance-based pressure conditions could be very useful in this sense.

Acknowledgements

This study was supported by the CIBER-BBN, an initiative funded by the VI National R&D&i Plan 2008–2011, Iniciativa Ingenio 2010, Consolider Program, CIBER Actions and financed by the Instituto de Salud Carlos III with assistance from the European Regional Development Fund and by the research project PI07/90023. The technical support of Plataform for Biological Tissue Characterization of the Centro de Investigación Biomédica en Red en Bioingeniería, Biomateriales y Nanomedicina (CIBER-BBN) is highly appreciated. We finally wish to thank Christine M. Scotti (W.L. Gore & Associates, Inc. Flagstaff, AZ, USA).

References

Balashazy I, Heistracher T, Hoffmann W. 1996. Air flow and particle deposition patterns in bronchial airway bifurcations: the effect of different CFD models and bifurcation geometries. J Aerosol Med. 9:287–301.

Bathe KJ. 2006. Theory and modeling guide. Vols I and II: ADINA and ADINA-F. Watertown, MA: ADINA R&D Inc.

Bathe KJ, Zhang H. 2002. A flow-condition-based interpolation finite element procedure for incompressible fluid flows. Comput Struct. 80(14–15):1267–1277.

Bathe KJ, Zhang H. 2004. Finite element developments for general fluid flows with structural interactions. Int J Numer Methods Eng. 60:213–232.

Brouns M, Jayaraju ST, Lacor C, De Mey J, Noppen M, Vincken W, Verbanck S. 2007. Tracheal stenosis: a fluid dynamics study. J Appl Physiol. 102:1178–1184.

Brouns M, Verbanck S, Lacor C. 2007. Influence of glottic aperture on the tracheal flow. J Biomech. 40:165–172.

Calay RK, Kurujareon J, Holdo AE. 2002. Numerical simulation of respiratory flow patterns within human lungs. Respir Physiol Neurobiol. 130:201–221.

Cebral JR, Summers RM. 2004. Tracheal and central bronchial aerodynamics using virtual bronchoscopy and computational fluid dynamics. IEEE Trans Med Imaging. 23(8):1021–1033.

Comerford A, Bauer G, Wall WA. 2010. Nanoparticle transport in a realistic model of the tracheobronchial region. Int J Numer Methods Biomed Eng. 26:904–914.

Comerford A, Foerster C, Wall WA. 2010. Structured tree impedance outflow boundary conditions for 3D lung simulations. J Biomech Eng. 132:1–10.

Comer JK, Kleinstreuer C, Zhang Z. 2001a. Flow structures and particle deposition patterns in double-bifurcation airway models. Part 1. Air flow fields. J Fluid Mech. 435:25–54.

Comer JK, Kleinstreuer C, Zhang Z. 2001b. Flow structures and particle deposition patterns in double-bifurcation airway models. Part 2. Aerosol transport and deposition. J Fluid Mech. 435:55–80.

Corcoran TE, Chigier N. 2000. Characterization of the laryngeal jet using phase Doppler interferometry. J Aerosol Med. 13(2):125–137.

Dumon F. 1990. A dedicated tracheobronchial stent. Chest. 97:328–332.

Elad D, Shochat A, Shiner RJ. 1998. Computational model of oscillatory airflow in a bronchial bifurcation. Respir Physiol Neurobiol. 112:95–111.

Evans DJ, Green M. 1998. Small airways: a time to revisit? Thorax. 53:629–630.

Freitas RK, Schröder W. 2008. Numerical investigation of the three-dimensional flow in a human lung model. J Biomech. 41:2446–2457.

Gemci T, Ponyavin V, Chen Y, Chen H, Collins R. 2008. Computational model of airflow in upper 17 generations of human respiratory tract. J Biomech. 41:2047–2054.

Habib RH, Chalker RB, Suki B, Jackson AC. 1994. Airway geometry and wall mechanical properties estimated from subglottal input impedance in humans. J Appl Physiol. 77(1):441–451.

Hazel AL, Heil M. 2003. Three-dimensional airway reopening: the steady propagation of a semi-infinite bubble into a buckled elastic tube. J Fluid Mech. 478:47–70.

Heil M. 1999. Airway closure: liquid bridges in strongly buckled elastic tubes. J Biomech Eng (ASME). 121:487–493.

Heil M, White JP. 2002. Airway closure: surface-tension-driven non-axisymmetric instabilities of liquid-lined elastic rings. J Fluid Mech. 462:79–109.

Horsfield K, Woldenberg MJ. 1989. Diameter of cross sectional areas of branches in the human pulmonary arterial tree. Anat Rec. 223:245–251.

Horsfield K, Dart G, Olson DE, Filley GF, Cumming G. 1971. Model of the human bronchial tree. J Appl Physiol. 31:207–217.

Jayaraju ST, Bronus M, Verbanck S, Lacor C. 2007. Fluid flow and particle deposition analysis in a realistic extrathoracic airway model using unstructured grids. J Aerosol Sci. 38:494–508.

Kim CS, Iglesias AJ. 1989. Deposition of inhaled particles in bifurcating airway models: I. Inspiratory deposition. J Aerosol Med. 2:1–14.

Kim CS, Iglesias AJ, Garcia L. 1989. Deposition of inhaled particles in bifurcating airway models: II. Expiratory deposition. J Aerosol Med. 2:15–27.

Koombua K, Pidaparti RM. 2008. Inhalation induced stresses and flow characteristics in human airways through fluid–structure interaction analysis. Model Simul Eng. (1–8):2008.

Latourelle JC, Gillis HL, Lutchen R. 2001. Exact motphometric modeling of rat lungs for predicting mechanical impedance. Respir Physiol. 127:75–85.

Levitzky MG. 2003. Pulmonary physiology. 7th ed. USA: McGraw-Hill. ISBN: 978-0-07-143775-2, MHID: 0-07-143775-4.

Lindenmann J, Porubsky C, Matzi V, Maier A, Smolle-Juettner FM. 2006. Inherent problems of tracheo-bronchial stenting in patients with tracheostomy. Ann Thorac Surg. 82:1897–1898.

Lin CL, Tawhai MH, McLennanc G, Hoffman EA. 2007. Characteristics of the turbulent laryngeal jet and its effect on airflow in the human intra-thoracic airways. Respir Physiol Neurobiol. 157:295–309.

Liu Y, So RMC, Zhang CH. 2002. Modeling the bifurcation flow in a human lung airway. J Biomech. 35:465–473.

Liu Y, So RMC, Zhang CH. 2003. Modeling the bifurcation flow in an asymmetric human lung airway. J Biomech. 36:951–959.

Li Z, Kleinstreuer C, Zhang Z. 2007. Particle deposition in the human tracheobronchial airways due to transient inspiratory flow patterns. Aerosol Sci. 38:625–644.

Luo HY, Liu Y. 2008. Modeling the bifurcating flow in a CT-scanned human lung airway. J Biomech. 41:2681–2688.

Ma B, Lutchen KR. 2006. An anatomically based hybrid computational model of the human lung and its application to low frequency oscillatory mechanics. Ann Biomed Eng. 34(11):1691–1704.

Macklem P. 1998. The physiology of small airways. Am J Respir Crit Care Med. 157:S181–S183.

Malvè M, Pérez del Palomar A, Lopez-Villalobos JL, Ginel A, Doblaré M. 2010. FSI analysis of the coughing mechanism in a human trachea. Ann Biomed Eng. 38(4): 1556–1565.

Malvè M, Pérez del Palomar A, Trabelsi O, Lopez-Villalobos JL, Ginel A, Doblaré M. 2011. Modeling of the fluid–structure interaction of a human trachea under different ventilation conditions. Int Commun Heat Mass Trans. 38:10–15.

Malvè M, Pérez del Palomar A, Chandra S, Lopez-Villalobos JL, Mena A, Finol EA, Ginel A, Doblaré M. 2011. FSI analysis of a healthy and a stenotic human trachea under impedance-based boundary conditions. J Biomech Eng. 33:1–12.

Malvè M, Pérez del Palomar A, Mena A, Trabelsi O, Lopez-Villalobos JL, Ginel A, Doblaré M. 2011. Numerical Modeling of a human stented trachea under different stent designs. Int Commun Heat Mass Trans. 38(7):855–862.

Malvè M, Pérez del Palomar A, Chandra S, Lopez-Villalobos JL, Finol EA, Ginel A, Doblaré M. 2011. FSI analysis of a human trachea before and after prosthesis implantation. J Biomech Eng. 133:1–12.

Matida EA, Finlay WH, Lange CF, Grgic B. 2004. Improved numerical simulation of aerosol deposition in an idealized mouth–throat. Aerosol Sci. 35:1–19.

Matida EA, Finlay WH, Breuer M, Lange C. 2006. Improving prediction of aerosol deposition in an idealized mouth using large-eddy simulation. J Aerosol Med. 19(3):290–300.

McCool DF. 2006. Global physiology and pathophysiology of cough ACCP evidence-based clinical practice guidelines. Chest, American College of Chest Physicians. 129:48–53.

Murray CD. 1926. The physiological principle of minimum work, the vascular system and the cost of blood volume. Proc Natl Acad Sci USA. 12:207–214.

Nithiarasu P, Hassan O, Morgan K, Weatherill NP, Fielder C, Whittet H, Ebden P, Lewis KR. 2008. Steady flow through a realistic human upper airway geometry. Int J Numer Methods Fluids. 57:631–651.

Nowak N, Kakade PP, Annapragada AV. 2003. Computational fluid dynamics simulation of airflow and aerosol deposition in human lungs. Ann Biomed Eng. 31:374–390.

Oertel H, Jr. 2004. Prandtl's essentials of fluid mechanics. Braunschweig/Wiesbaden, Germany: Springer.

Olufsen MS. 1999. A structured tree outflow condition for blood flow in larger systemic arteries. Am J Physiol – Heart Circ Physiol. 276:H257–H268.

Olufsen MS, Peskins CS, Kim WY, Pedersen EM, Nadim A, Larsen J. 2000. Numerical simulation and experimental validation of blood flow in arteries with structured tree outflow conditions. Ann Biomed Eng. 28:1281–1299.

Raabe OG, Yeh HC, Schum GM, Phalen RF. 1976. Tracheobronchial geometry: human, dog, rat, hamster. LF-53 Albuquerque, NM: Lovelace Fundation for Medical Education and Research.

Roberts CR, Rains JK, Paré PD, Walker DC, Wiggs B, Bert JL. 1998. Ultrastructure and tensile properties of human tracheal cartilage. J Biomech. 31:81–86.

Sera T, Satoh S, Horinouchi H, Kobayashi K, Tanishita K. 2003. Respiratory flow in a realistic tracheostenosis model. J Biomech Eng. 125:461–471.

Steele BN, Olufsen MS, Taylor CA. 2007. Fractal network model for simulating abdominal and lower extremity blood flow during resting and exercise conditions. Comput Methods Biomech Biomed Eng. 10(1):37–51.

Suki B, Habib RH, Jackson AC. 1993. Wave propagation, input impedance, and wall mechanics of the calf trachea from 16 to 1,600 Hz. Am J Physiol. 75:2755–2766.

Sun F, Uson J, Ezquerra J, Crisostomo V, Luis L, Maynar M. 2008. Endotracheal stenting therapy in dogs with tracheal collapse. Vet J. 175:186–193.

Tawhai MH, Hunter P, Tschirren J, Reinhardt J, McLennan G, Hoffman EA. 2004. CT-based geometry analysis and finite element models of the human and ovine bronchial tree. J Appl Physiol. 97:2310–2321.

Wall WA, Rabczuk T. 2008. Fluid–structure Interaction in lower airways of CT-based lung geometries. Int J Numer Meth Fluids. 57:653–675.

Wall WA, Wiechert L, Comerford A, Rausch S. 2010. Towards a comprehensive computational moel for the respiratory system. Int J Numer Methods Biomed Eng. 26: 807–827.

Weibel ER. 1963. Morphometry of the human lung. New York: Academic Press.

White JP, Heil M. 2005. Three-dimensional instabilities of liquid-lined elastic tubes: a lubrication theory model. Phys Fluids. 17(3):031506–031517.

Xi J, Longest PW. 2007. Transport and deposition of micro-aerosols in realistic and simplified models of the oral airway. Ann Biomed Eng. 35(4):560–581.

Xi J, Longest PW. 2008. Evaluation of a novel drift flux model for simulating submicrometer aerosol dynamics in human upper tracheobronchial airways. Ann Biomed Eng. 36(10):1714–1734.

Xi J, Longest PW, Martonen TB. 2008. Effects of the laryngeal jet on nano- and microparticle transport and deposition in an

approximate model of the upper tracheobronchial airways. J Appl Physiol. 104:1761–1777.

Xia G, Tawhai MH, Hoffman EA, Lin C. 2010. Airway wall stiffening increases peak wall shear stress: a fluid–structure interaction study in rigid and compliant airways. Ann Biomed Eng. 38(5):1836–1853.

Yang XL, Liu Y, So RMC, Yang JM. 2006. The effect of inlet velocity profile on the bifurcation COPD airway flow. Comput Biol Med. 36:181–194.

Yeh HC, Schum GM, Duggan MT. 1979. Anatomic models of the tracheobronchial and pulmonary regions of the rat. Anat Rec. 195:483–492.

Zamir M. 2000. The physics of pulsatile flow. Biological physics series, New York: Springer.

Zhang Z, Kleinstreuer C. 2002. Transient airflow structures and particle transport in a sequentially branching lung airway model. Phys Fluids. 14:862–880.

Zhang Z, Lessmann R. 1996. Computer simulation of the flow field and particle deposition by diffusion in a 3-d human airway bifurcation. Aerosol Sci Technol. 25:338–352.

Zhang Z, Kleinstreuer C, Kim CS. 2002. Micro-particle transport and deposition in a human oral airway model. Aerosol Sci. 33:1635–1652.